Earth's Future

Key Points:

- We apply a modification of the joint probability Bayesian quadrature approach for compound rainfall-surge flood hazard
- Using peak rain rate, peak storm tide, and relative time lag as joint probability parameters accurately captures historical flood hazard
- Sea-level rise and tropical cyclone climatology change increases 100-year flood extent by 27% and flood volume by 62% in the Cape Fear Estuary catchment

Correspondence to:

A. Gori,
agori@princeton.edu

Projecting Compound Flood Hazard Under Climate Change With Physical Models and Joint Probability Methods

Avantika Gori[1] (ID) **and Ning Lin[1]** (ID)

[1]Department of Civil and Environmental Engineering, Princeton University, Princeton, NJ, USA

Abstract Accurate delineation of compound flood hazard requires joint simulation of rainfall-runoff and storm surges within high-resolution flood models, which may be computationally expensive. There is a need for supplementing physical models with efficient, probabilistic methodologies for compound flood hazard assessment that can be applied under a range of climate and environment conditions. Here we propose an extension to the joint probability optimal sampling method (JPM-OS), which has been widely used for storm surge assessment, and apply it for rainfall-surge compound hazard assessment under climate change at the catchment-scale. We utilize thousands of synthetic tropical cyclones (TCs) and physics-based models to characterize storm surge and rainfall hazards at the coast. Then we implement a Bayesian quadrature optimization approach (JPM-OS-BQ) to select a small number (~100) of storms, which are simulated within a high-resolution flood model to characterize the compound flood hazard. We show that the limited JPM-OS-BQ simulations can capture historical flood return levels within 0.25 m compared to a high-fidelity Monte Carlo approach. We find that the combined impact of 2100 sea-level rise (SLR) and TC climatology changes on flood hazard change in the Cape Fear Estuary, NC will increase the 100-year flood extent by 27% and increase inundation volume by 62%. Moreover, we show that probabilistic incorporation of SLR in the JPM-OS-BQ framework leads to different 100-year flood maps compared to using a single mean SLR projection. Our framework can be applied to catchments across the United States Atlantic and Gulf coasts under a variety of climate and environment scenarios.

Plain Language Summary When storm surges and heavy rainfall co-occur in coastal areas their impacts can compound to exacerbate overall flooding. To adequately prepare for coastal floods, it is necessary to delineate areas that have a higher probability to flood, often referred to as flood hazard maps. However, accurate delineation of flood hazard requires jointly simulating rainfall and storm surges within high-resolution physical models, which may be computationally expensive. Here we propose an extension to the joint probability method with optimal sampling, to allow computationally efficient delineation of compound flood hazard. Our method utilizes thousands of synthetic tropical cyclones (TCs) to characterize the joint probability of rainfall and storm surges, and Bayesian quadrature to select a relatively small number (~100) of storms that are simulated within a high-resolution physical inundation model. We apply our approach to the Cape Fear Estuary, NC to delineate historical and future flood hazard under the combined influence of sea-level rise (SLR) and changing TC climatology. SLR and TC climatology change may cause a 27% increase in the 100-year flood extent and a 62% increase in the 100-year flood volume. We demonstrate that a probabilistic treatment of SLR produces different flood hazard maps compared to using a single SLR scenario.

1. Introduction

Coastal regions are highly vulnerable to severe flooding (Hallegatte et al., 2013; Woodruff et al., 2013), which may be caused by storm surges (e.g., Kirezci et al., 2020; Muis et al., 2016), high river discharges (e.g., Ikeuchi et al., 2015), intense precipitation (e.g., Bass et al., 2016; Wang et al., 2016), or a combination of multiple flood drivers (e.g., Couasnon et al., 2019; Lai et al., 2021; Ward et al., 2018). The joint or consecutive occurrence of these flood mechanisms within a coastal catchment can exacerbate overall flooding, resulting in a compound flood (Zscheischler et al., 2020). Along the coastline of the United States (US), tropical cyclones (TCs) and extra-tropical cyclones (ETCs) can both cause concurrent heavy rainfall and high storm surges (Lai et al., 2021; Orton et al., 2018; Wahl et al., 2015), making them dominant drivers of compound floods. While ETCs tend to cause more frequent, moderate floods, TCs are more likely to cause extreme flooding (Booth et al., 2016; Lai et al., 2021; Orton et al., 2018; Smith et al., 2011; Villarini et al., 2014). For example, Hurricane Florence (2018) caused a roughly 100-year storm tide in the Cape Fear River, NC while simultaneously dropping rainfall totals

that exceeded the 500-year level (Stewart and Berg, 2018). Moreover, the dependence structure between rainfall and storm surges may be different for TCs compared to ETCs (Kim et al., 2022). Therefore, to adequately characterize coastal flood risk, it is crucial to specifically account for the dependence between TC rainfall and storm surges and jointly model their flood impacts in coastal catchments.

As sea levels continue to rise throughout the 21st century and North Atlantic TCs potentially become more intense (Knutson et al., 2020), compound flooding is likely to become worse. Sea-level rise (SLR) worsens flooding by increasing the base ocean water level upon which the storm surge acts and by preventing efficient freshwater drainage from coastal catchments. Climate-induced changes in TC climatology, such as increasing intensity and decreasing translation speed, may increase peak storm surges and rainfall accumulations at the coast (Gori et al., 2022; Kossin, 2018; Liu et al., 2019). Consequently, projected SLR and storm climatology changes due to future climate change should be incorporated in compound flooding analysis to provide a long-term view of coastal hazard.

Flood hazard is typically quantified in terms of inundation maps that relate maximum water depth to exceedance probabilities (i.e., return periods), and compound flood maps take into account the joint occurrence of rainfall-runoff and storm surge flooding. Methodologies for generating compound flood maps typically first characterize the joint probability distribution of multiple flood drivers (such as rainfall and storm surge or river discharge and storm surge) and then develop a set of flood mapping scenarios based on the joint distribution (Couasnon et al., 2018; Lian et al., 2013; Ming et al., 2022; Moftakhari et al., 2019; van den Hurk et al., 2015; Zellou and Rahali, 2019). However, the process of developing flood scenarios is not trivial and often requires making several assumptions about the spatial and temporal relationship between different flood drivers. For example, the relative time lag between peak rainfall and peak storm surge can significantly alter compound flooding extent (Gori, Lin, & Xi, 2020; Shen et al., 2019), but many studies simply assume the hazard peaks occur at the same time or evaluate a range of time lags (Bates et al., 2021; Moftakhari et al., 2019; Pasquier et al., 2018; Shen et al., 2019). It is usually not known whether different time lag assumptions are physically realistic. An alternate method to develop compound flood maps involves generating a large number of physics-based rainfall-surge events, using them as boundary conditions to simulate flooding within an inundation model, and estimating flood return levels based on the inundation simulations (Gori, Lin, & Xi, 2020). Although this method avoids making simplifying assumptions about the hazard inter-relationships, it is often computationally expensive and therefore not easily implemented for a variety of different climate and environment conditions. A third approach for compound flood hazard assessment involves training a statistical surrogate model using a range of rainfall-surge scenarios and output from a high-fidelity flood model. Then the surrogate model can be forced with many rainfall-surge realizations to estimate flood return levels (Bass & Bedient, 2018; Serafin et al., 2019). However, the surrogate model is location-specific and if future climate scenarios are more extreme than the initial training set, or if landscape conditions are forecast to change in the future, the surrogate model may need to be re-developed and/or re-trained. The limitations inherent to existing compound flood mapping approaches motivate the development of physics-based, efficient methodologies for high-resolution delineation of compound flood hazard.

Recently, a few studies (Bates et al., 2021; Bermúdez et al., 2021; Hamman et al., 2016; Hsiao et al., 2021; Khanam et al., 2021) have analyzed changes in compound flood hazard due to projected climate change, although most have relied on deterministic scenarios rather than probabilistic analysis to evaluate the impact of projected changes in sea-level and rainfall. Previous studies typically consider only a limited set of deterministic SLR scenarios (Bates et al., 2021; Bermúdez et al., 2021; Hamman et al., 2016; Khanam et al., 2021) in their analysis of future flood hazard and do not incorporate SLR projections probabilistically. Since projected rates of SLR are highly uncertain, with non-negligible probability for extreme SLR to occur by 2100 (Kopp et al., 2014, 2017), incorporating SLR probabilistically within flood mapping frameworks can propagate these large uncertainties and avoid the ambiguity of selecting particular SLR levels. Moreover, previous flood mapping studies do not capture projected changes in the dependence structure between rainfall and storm surges (Gori et al., 2022; Wahl et al., 2015), which could impact compound flood depths.

In this study we propose a framework for quantifying compound flood hazard at the catchment-scale under current and future storm climatology and sea-level that relies on physics-based synthetic hazard events and an extension of the joint probability method with optimal sampling (JPM-OS; FEMA, 2012; Ho and Myers, 1975). Specifically, we utilize a large number of downscaled synthetic TCs whose rainfall fields and storm tides are simulated

using high-resolution, physics-based models. Using the modeled rainfall, storm tides, and their relative time lag, we implement the joint probability optimal sampling method (JPM-OS) method with Bayesian Quadrature to select a relatively small number (∼85–120) of events, which are simulated within a high-resolution compound flood model. Modeled flood maps from the selected storms are used to quantify flood return levels ranging from 10 to 250 years. We quantify compound flood hazard under historical climate conditions (1980–2005) based on reanalysis data, future storm climatology conditions (high emission scenario SSP5 8.5 from 2070 to 2100) based on downscaled storms from eight CMIP6 general circulation models (GCMs), and we incorporate 2100 projected SLR (high emission scenario RCP 8.5) by adding sea-level as an additional JPM-OS parameter. We apply our compound flood mapping approach to the Cape Fear River Estuary, NC, which is highly vulnerable to compound flooding from TC events (Gori, Lin, & Smith, 2020).

2. Methods

The general approach for simulating compound flood hazard under historical and future projected conditions involves five main steps. First, synthetic TCs are downscaled using a statistical-deterministic model forced with either reanalysis (for historical period) or GCM (for future period) data. Approximately 1000 storms are downscaled for the historical period and 10,000 storms for the future period (from the eight different GCMs). Rainfall fields for each synthetic TC are simulated using a physics-based TC rainfall model. Storm tides are simulated using a basin-scale hydrodynamic model. The simulations associated with step one were conducted in Gori et al. (2022) and we utilize the modeled results here. In step two, TC hazard parameters (i.e., peak rainfall, peak storm tide, time lag) and SLR (in the future case) are input to a modified JPM-OS Bayesian Quadrature (JPM-OS-BQ) algorithm to select a smaller number (∼100) of representative storms and calculate their associated probabilities. The reduced storm set spans the multivariate probability space of the rainfall, storm tides, and hazard time lags. In step three, which is only necessary for the future case, the selected storms are simulated again within the hydrodynamic storm tide model using the associated SLR values as an initial water level offset to account for nonlinear interactions between storm tide and SLR. In step four, the modeled rainfall fields and storm tide time series for each of the selected storms are input to a high-resolution flood model and maximum inundation depths are simulated. Finally, in step five the simulated maximum flood depths from the high-resolution flood model are combined with the JPM-OS-BQ storm probabilities to derive flood return level maps ranging from 10-years to 250-years. The compound flood hazard approach is applied to the Cape Fear River Estuary in North Carolina, USA.

2.1. Study Area—Cape Fear River

The Cape Fear River flows eastward through North Carolina, becoming a tidally influenced estuary at the coast (Figure 1, inset). The entire Cape Fear basin drains approximately one third of the state and the river extends over 322 km. However, tides only propagate roughly 100 km upstream from the mouth of the river (Famikhalili & Talke, 2016) and consequently the compound flood threat is highest for the near-coast portion of the river/estuary. The Cape Fear River has experienced multiple compound floods from historical TCs, including during Hurricanes Fran (1996) and Floyd (1999), and more recently from Hurricane Florence (2018). During these historical TCs, intense rainfall caused widespread flooding of overland areas and small tributaries while high storm surges caused elevated water levels within the Cape Fear River and blocked drainage of rainfall-runoff, exacerbating overall flooding (Gori, Lin, & Smith, 2020; Ye et al., 2021). To focus on compound flood dynamics near the coast, we model flooding from the mouth of the river to 40 km upstream using a high-resolution inundation model and capture upstream river flows using a regional hydrologic model.

2.2. Synthetic TCs and Hazard Models

Synthetic TCs for the historical period (1980–2005) were downscaled in Gori et al. (2022) using the statistical-deterministic model of Emanuel et al. (2006), forced with National Centers for Environmental Prediction (NCEP) reanalysis data (Kalnay et al., 1996). The model randomly seeds vortices, which are then moved according to perturbations of the reanalysis-based climatology of steering flows plus a beta-drift correction (G. J. Holland, 1983). The TC intensity is calculated at 2-hourly time steps using a deterministic axisymmetric vortex model (Emanuel et al., 2004). The seeding rate of TC vortices is calibrated so that TC occurrences match the
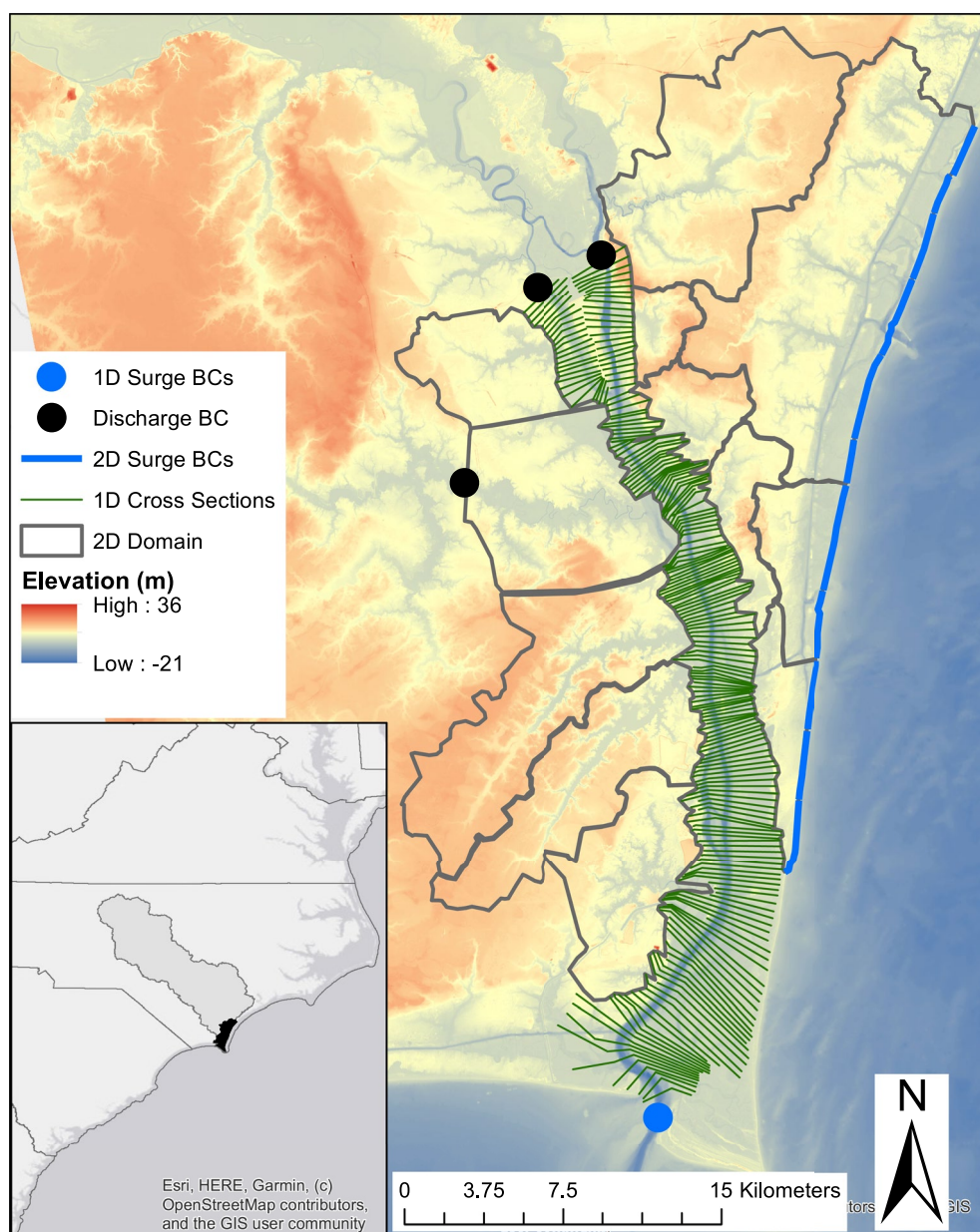
Figure 1. Study area and inundation model domain showing ocean and river boundary condition locations. Cape Fear drainage basin shown in light gray, and high-resolution model domain shown in black (inset).

observed yearly TC frequency in the North Atlantic basin. For the future period from 2080 to 2100 we utilize downscaled TCs from the same statistical-deterministic model based on output from eight CMIP6 GCMs under the high emission scenario (SSP 5 8.5). Here we focus on the highest emission scenario to examine a worst-case future flood hazard that is consistent with historical CO_2 emissions (Schwalm et al., 2020). However, the same modeling framework could be applied using the moderate SSP2 4.5 scenario. 5,018 synthetic tracks across the North Atlantic basin were generated for the historical period and 6,200 tracks for each CMIP6 model were generated for the future period. We select all tracks passing within 200 km of the Cape Fear River Estuary, resulting in 941 tracks in the historical period and 1,175 tracks in the future period. In addition to the synthetic tracks, the TC model also projects the basin-wide yearly TC frequency based on the GCM data. The model projects a large increase in TC frequency for some CMIP6 GCMs under the SSP 5 8.5 scenario (Gori et al., 2022), which contrasts with the findings from the majority of previous studies (Knutson et al., 2020). Given the large uncer-

tainty in TC frequency change projections (Sobel et al., 2021), here we assume no change in basin-wide TC frequency for the future period. The intensity distributions of future TCs from each GCM are bias corrected using a re-weighting approach (Gori et al., 2022) according to their match to the reanalysis-based TCs in the historical period. Then, each GCM is weighted based on its performance on simulating the storm intensity distribution in the historical period, and storms from each GCM are combined to produce a single composite storm set of 9,400 storms (see Gori et al., 2022 for details) used in this study.

Rainfall fields for each TC are modeled using the TC Rainfall (TCR) model (Lu et al., 2018; Zhu et al., 2013), which is a simplified, physics-based convective model that has been widely applied for rainfall hazard assessment (Feldmann et al., 2019; Xi et al., 2020; Zhu & Quiring, 2013) and flood hazard assessment (Gori, Lin, & Xi, 2020; Lu et al., 2018; Zhu et al., 2021). The TCR model formulation and performance for historical TCs are documented in Zhu et al. (2013), Lu et al. (2018), and Xi et al. (2020). Storm tides from each TC are simulated using parametric wind and pressure models (Emanuel & Rotunno, 2011; G. Holland, 1980) as forcing within the depth-integrated version of the Advanced Circulation (ADCIRC; Luettich et al., 1992; Westerink et al., 1992) hydrodynamic model. We use a basin-scale mesh developed in Marsooli and Lin (2018) with a coastal resolution of ∼1 km and incorporate eight tidal constituents in our storm tide simulations. To simulate future ocean conditions in 2100, we incorporate probabilistic, localized SLR projections from Kopp et al. (2014) under the RCP 8.5 high-emission scenario (equivalent to the SSP5 8.5 scenario).

2.3. JPM-OS for Compound Flooding

The Joint Probability Method (JPM; Ho & Myers, 1975; Myers, 1975) was developed in the 1970s as an approach for estimating coastal storm surge return period levels by relating the surge exceedance probability to the integral of the joint probability of hurricane storm characteristics at landfall. Typically, the storm characteristics incorporated in the JPM are intensity (i.e., minimum central pressure—P_{min}), radius to maximum winds (R_{max}), forward speed (V_f), approach angle (θ), and landfall location. Within the JPM framework, the yearly maximum storm surge (η_{max}) distribution can be estimated as:

$$P(\eta_{max} > \eta) = \lambda \int \dots \int_{x} f_X(x) P(\eta_m(x) > \eta) \, dx \tag{1}$$

where λ is the yearly TC frequency, x is a m-dimensional variable of storm characteristics at landfall, $f_X(x)$ is the joint probability density function of the storm characteristics and $P(\eta_m(x) > \eta)$ is the conditional probability function that a storm with x characteristics causes a modeled peak storm surge ($\eta_m(x)$) greater than a certain flood elevation (η). If the storm surge model is assumed to be a perfect representation of the true peak storm surge, then $P(\eta_m(x) > \eta)$ simplifies to a Heaviside step function. Directly computing Equation 1 involves modeling the peak storm surge for all possible combinations of storm characteristics, which is too computationally expensive in most applications. Subsequent variations of the JPM have allowed for computationally efficient calculation of the joint integral through optimal sampling, response functions, and/or quadrature (JPM-OS; Irish et al., 2009; Niedoroda et al., 2008; Resio et al., 2009). In particular, Bayesian Quadrature (Toro, Niedoroda, et al., 2010) has been widely applied to approximate the joint probability integral using a limited number of storm scenarios and analytically calculated weights for each storm (Niedoroda et al., 2008; Toro, Niedoroda, et al., 2010, Toro, Resio, et al., 2010). Here, we extend the JPM-OS-BQ approach to estimate compound flood hazard from coastal rainfall and storm tides.

The Bayesian Quadrature approach approximates the integral in Equation 1 as a weighted summation of the form:

$$P(\eta_{max} > \eta) \approx \lambda \sum_{i=1}^{n} w_i P(\eta_m(x_i) > \eta) \tag{2}$$

where x_i is the ith selected storm and w_i is the analytically calculated weight (probability) for storm i. The function $P(\eta_m(x) > \eta)$ in Equation 1 is idealized as an m-dimensional Gaussian process whose expected value (mean) conditioned on a set of known nodal values (i.e., $P(\eta_m(x_1) > \eta)$, $P(\eta_m(x_2) > \eta)$, ... $P(\eta_m(x_i) > \eta)$) is a linear combination of the nodal values, and the linear coefficients depend on the specified autocovariance function

($k(\boldsymbol{x}, \boldsymbol{y})$; a double-exponential form is used here following Toro, Niedoroda, et al., 2010) for the process. The double-exponential autocovariance function used here and in previous studies has the form:

$$k\left(\boldsymbol{x}_i, \boldsymbol{y}_i\right) = \prod_{j=1}^{m} \exp\left[-\left(\frac{x_{i,j} - y_{i,j}}{c_j}\right)^2\right] \tag{3}$$

where $\boldsymbol{x}_i$ and $\boldsymbol{y}_i$ denote two points in the m-dimensional parameter space and the subscript j denotes the dimension ranging from 1 to m. c_j represents the user-specified correlation distance in each dimension, which controls the rate at which the correlation decays along dimension j. In general, variables that are more important should have smaller specified correlation distances so that the optimization algorithm spaces the storm points more closely together. The correlation distances can be specified based on the results from previous studies (Niedoroda et al., 2008; Toro, Niedoroda, et al., 2010; Toro, Resio, et al., 2010) and modified based on trial-and-error analysis. Given a set of n support points (i.e., number of synthetic storms whose characteristics are represented in m-dimensional space) represented as an m by n dimensional matrix ($\boldsymbol{D}$), the vector of weights ($\boldsymbol{W}$) are calculated by solving a system of equations involving the joint density ($f_X(\boldsymbol{x})$ in Equation 1) and the autocorrelation function ($k(\boldsymbol{x}, \boldsymbol{y})$):

$$\boldsymbol{W} = U(\boldsymbol{x}, \boldsymbol{D})^T K^{-1}(\boldsymbol{D}, \boldsymbol{D}) \tag{4}$$

$$U(\boldsymbol{x}, \boldsymbol{D}) = \begin{vmatrix} \int_{\boldsymbol{x}} k(\boldsymbol{x}, \boldsymbol{x}_1) f_X(\boldsymbol{x}) d\boldsymbol{x} \\ \vdots \\ \int_{\boldsymbol{x}} k(\boldsymbol{x}, \boldsymbol{x}_n) f_X(\boldsymbol{x}) d\boldsymbol{x} \end{vmatrix} \tag{5}$$

$$K(\boldsymbol{D}, \boldsymbol{D}) = \begin{bmatrix} k(\boldsymbol{x}_1, \boldsymbol{x}_1) & \cdots & k(\boldsymbol{x}_1, \boldsymbol{x}_n) \\ \vdots & \ddots & \vdots \\ k(\boldsymbol{x}_n, \boldsymbol{x}_1) & \cdots & k(\boldsymbol{x}_n, \boldsymbol{x}_n) \end{bmatrix} \tag{6}$$

The integral in U ($\boldsymbol{x}, \boldsymbol{D}$) may be equally difficult to compute as the original integral in Equation 1. However, when the autocorrelation function is specified as a double exponential equation (as is the case here) and the joint density function in the optimization space is specified as a multivariate normal distribution, the integral of their product (Equation 5) can be calculated analytically, allowing the nodal weights to be computed efficiently (see subsequent section for more details). A full derivation of the equations for the weights is presented in Toro, Niedoroda, et al. (2010) and Minka (2000). To select the optimal storm support points, the JPM-OS-BQ algorithm seeks to minimize the variance of the integration error, which is only based on the autocorrelation function and joint density and can therefore be calculated without having to repeatedly simulate the flood heights within the computationally expensive flood model. The optimization procedure involves an iterative loop where n storms are chosen each time, their weights and associated estimation variance are calculated, and then an adjusted set of storms is chosen for the next iteration. We utilize the NEWUOA numerical optimization algorithm developed by Powell (2004) as in previous JPM-OS-BQ studies (Niedoroda et al., 2008; Toro, Resio, et al., 2010; Yin et al., 2018).

We apply two approaches with the JPM-OS-BQ method for compound flood hazard estimation. In the first approach, we utilize TC storm characteristics of maximum sustained wind speed (V_{max}), R_{max}, V_f, and minimum distance to the study area (MinD) to construct the joint density function, similar to previous studies that have applied JPM-OS-BQ for storm surge hazard. We selected the four parameters based on lasso regression (Friedman et al., 2010) using a larger set of potential parameters to predict peak storm surge and peak rainfall rate. We chose all parameters with non-zero regression coefficients for at least one of the two regression models, assuming a parsimonious model where the mean square error is less than one standard deviation higher than the best model. Using this approach, we select storm characteristics that are correlated with either peak storm surge and peak rainfall rate or both, and thus are likely to provide a reasonable representation of the compound flood hazard. The storm parameters we select based on the lasso regression are similar to the storm parameters used in many previous JPM-OS studies (Bilskie et al., 2019; Niedoroda et al., 2008; Toro, Niedoroda, et al., 2010). Therefore, in the absence of pre-simulated rainfall and storm tide data, the storm parameters could be specified based

on the set up from previous studies. In the second approach, we directly utilize modeled peak storm tide, peak rainfall rate, and the relative time lag between the hazards to represent the joint density. The second approach is hypothesized to yield more accurate compound flood hazard results since it directly utilizes the probability distributions of each flood driver rather than relying on storm characteristics as proxy variables. The storm tide and rainfall simulations are less computationally expensive in comparison to the high-resolution flood model, and thus it is feasible to simulate the storm tides and rainfall fields associated with thousands of synthetic TCs under various climate conditions (e.g., see Gori et al., 2022; Lin et al., 2012; Marsooli et al., 2019). Moreover, there are several existing databases of simulated TC hazards from synthetic storms (Bloemendaal et al., 2020; Gori et al., 2022; Muis et al., 2016) that could be used in future studies as input to the JPM-OS-BQ method. We compare our compound flood maps derived from the JPM-OS-BQ method against flood maps that were generated in Gori, Lin, and Xi (2020) using a Monte Carlo (MC) approach that simulated all 941 historical NCEP TCs within the high-resolution flood model. We evaluate the performance of each test case by its ability to match the MC-based flood maps for a range of return periods (25–250 years).

2.3.1. Approach 1: TC Storm Characteristics for Compound Flood Estimation

In the first approach, we utilize storm characteristics of V_{max}, V_f, R_{max}, and MinD and estimate their joint probability density function. The distribution of V_{max} is characterized by a heavy upper tail, indicating that extreme intensity TCs occur with non-negligible frequency in the study area. Consequently, the tail of the V_{max} distribution is modeled using a generalized pareto distribution (Lombardo et al., 2009) and the rest of the distribution is represented using a kernel density function. The storm V_f is best fit by a Weibull distribution, as in previous work (Condon & Sheng, 2012). The storm R_{max} is negatively correlated with V_{max} since weaker storms tend to have larger R_{max} and stronger storms have smaller R_{max}. Therefore, we represent the R_{max} density function as a normal distribution whose parameters are a function of V_{max}, similar to previous studies (e.g., Irish and Resio, 2013). We subset the synthetic storms into bins based on their V_{max} at landfall and calculate the mean and variance of R_{max} within each bin to obtain the parameters for the R_{max} distribution. The final parameter, MinD, is represented as a uniform distribution from 0 to 200 km (we only select storms passing within 200 km of the study area) since the empirical MinD distribution of the synthetic storms closely resembled a uniform distribution. We assume V_{max} and R_{max} are the only correlated variables since all other variable pairs were not statistically significantly correlated in the synthetic storm set.

The JPM-OS-BQ optimization requires repeated calculations of the integral of the joint density times the autocorrelation function (see Equation 5). Since the joint density is normal for some variables, non-normal for others, and because some of the variables are correlated, it would be computationally costly to numerically compute the integral in the physical parameter space. To overcome this challenge, previous studies (Nadal-Caraballo et al., 2015; Niedoroda et al., 2008; Sheng et al., 2022; Toro, Niedoroda, et al., 2010; Toro, Resio, et al., 2010; Yin et al., 2018) have used the Rosenblatt transformation (Rosenblatt, 1952) to convert the joint density from the physical parameter space to an equivalent uncorrelated, normal space (which we call the optimization space). Conversion of the joint density to an uncorrelated joint normal distribution allows analytical computation of Equation 5, thereby ensuring computational efficiency of the optimization algorithm. In previous applications, the joint density is sliced into bins according to the Saffir-Simpson category scale, and the storm intensity is assumed normal within each slice (Nadal-Caraballo et al., 2015; Niedoroda et al., 2008; Toro, Niedoroda, et al., 2010; Yin et al., 2018). Here, we eliminate the need for pre-slicing by representing the distribution of V_{max} in the optimization space using a normal mixture model capable of representing the heavy upper tail. The choice of normal mixture model allows the optimization algorithm to remain computationally efficient, since Equation 5 can still be computed analytically. Similar to V_{max}, the storm forward speed (V_f) is also characterized by a heavy upper tail and its density function is also represented by a mixture of two normal distributions in the optimization space. Using a two-component normal mixture distribution yields a density function of the form:

$$f(x) \sim \varphi N\left(\mu_1, \sigma_1^2\right) + (1 - \varphi) \text{N}\left(\mu_2, \sigma_2^2\right) \tag{7}$$

where $N\left(\mu, \sigma^2\right)$ is a normal density function with mean μ and variance σ^2 and φ is the mixing proportion that determines how much weight is applied to each normal distribution.

As the storm V_{max} is the most important parameter driving both the storm surge and the rainfall (Gori et al., 2022), we specify the smallest correlation distance ($c = 0.5$). MinD and R_{max} are given the second smallest correlation distances ($c = 1$), and V_f has the largest correlation distance ($c = 2$) due to its smaller effect on peak storm tide

(Resio et al., 2009). We implement the optimization algorithm on the NCEP historical storm data using 85 support points, based on trial-and-error analysis.

2.3.2. Approach 2: TC Hazards for Compound Flood Estimation

In the second approach, we directly utilize the simulated peak storm tides and peak rainfall rates from Gori et al. (2022), as well as the relative time lag between the hazard peaks within the JPM-OS-BQ algorithm. The peak storm tide and peak rainfall rate are highly correlated in this region (Gori, Lin, & Smith, 2020, Gori, Lin, & Xi, 2020) and we model their dependence in the physical space by fitting a bivariate copula. We use the VineCopula package in R (Schepsmeier et al., 2016), which considers 13 different copula types when fitting the dependence model and selects the best copula family based on the Akaike information criterion. The marginal distribution of both the peak storm tide and rainfall rate are represented using a generalized pareto distribution for the upper tail of the distribution and a kernel density function for the non-extreme portion of the distribution (Lin et al., 2010, 2012). The relative time lag between the hazard peaks is included as a third parameter because it was found to be a significant driver of compound flood severity in our previous study (Gori, Lin, & Xi, 2020). The time lag is distributed normally and is not significantly correlated with either peak rainfall or peak storm tide. In the optimization space, we fit a two-component normal mixture model to represent the peak storm tide and a normal distribution to the rainfall as it is distributed approximately normal conditioned upon peak storm tide.

Since both the peak storm tide and peak rainfall are important in driving overall flooding, each variable has a correlation distance of $c = 0.5$, while the correlation distance for time lag between hazards is set as $c = 2$, reflecting its smaller contribution to total flooding. As in the first approach, we implement the optimization algorithm on the NCEP historical storm data using 85 support points.

2.3.3. Application to Future Storm Climatology and SLR

After evaluating the two approaches using the historical NCEP data and comparing the results against the MC compound flood results, we then apply the second approach to simulate compound flood hazard under future storm climatology (2070–2100) and future SLR (2100). In this future case, the JPM-OS-BQ algorithm uses peak storm tide, peak rainfall rate, relative time lag, and SLR as the variables comprising the joint density function. The distributions of the first three variables are represented in the same manner as Approach 2, while SLR is incorporated as a fourth parameter that is assumed to be independent of the others. The distribution of SLR is specified in Kopp et al. (2014) and is characterized by a heavy upper tail representing extreme, but plausible future sea levels. Therefore, in the optimization space we model the SLR distribution as a two-component normal mixture. The correlation distances are set as $c = 0.5$ for the peak storm tide and rainfall rate, $c = 1$ for SLR, and $c = 2$ for the time lag. To adequately capture the heavy tail of both the storm tide and SLR distributions, we use a larger number of support points ($N = 120$) in the JPM-OS-BQ optimization.

After selecting a subset of storms using the JPM-OS-BQ algorithm, the selected storms are re-simulated in ADCIRC using their associated SLR values to account for the nonlinear impact of eustatic SLR on tides and storm surges (Arns et al., 2020). We incorporate SLR in ADCIRC by offsetting the initial model mean sea-level by a specific value, as in Bilskie et al. (2016). The re-simulated storm tides accounting for SLR are then used as boundary forcing for the high-resolution flood model.

2.4. High-Resolution Flood Model

Compound flooding is simulated using the Hydrologic Engineering Center (HEC) Riverine Analysis System (Hydrologic Engineering Center-Riverine Analysis System), which is a shallow water equation model (Brunner, 2016). We use a coupled 1D/2D approach where the main stem of the Cape Fear River is simulated using 1D cross sections and smaller tributaries and overland areas are simulated using a 2D, 60 m resolution mesh and 1 m sub-grid topography. The 1D and 2D portions of the model were previously validated in Gori, Lin, and Smith (2020) for six historical TC events using water level data from tidal gauges and high-water marks. The model jointly simulates flooding from storm tides, rainfall-runoff, and river discharges. Storm tides from ADCIRC are input as a 2D boundary condition with 1-hr temporal resolution along the coastline and at the mouth of the river (Figure 1). Rainfall fields simulated by the TCR model, which have a 0.05-degree horizontal resolution and 2-hr temporal resolution, are applied to the 2D model grid after subtracting infiltration according to the Green and Ampt (1911) equation. Upstream river discharges are simulated using a regional HEC
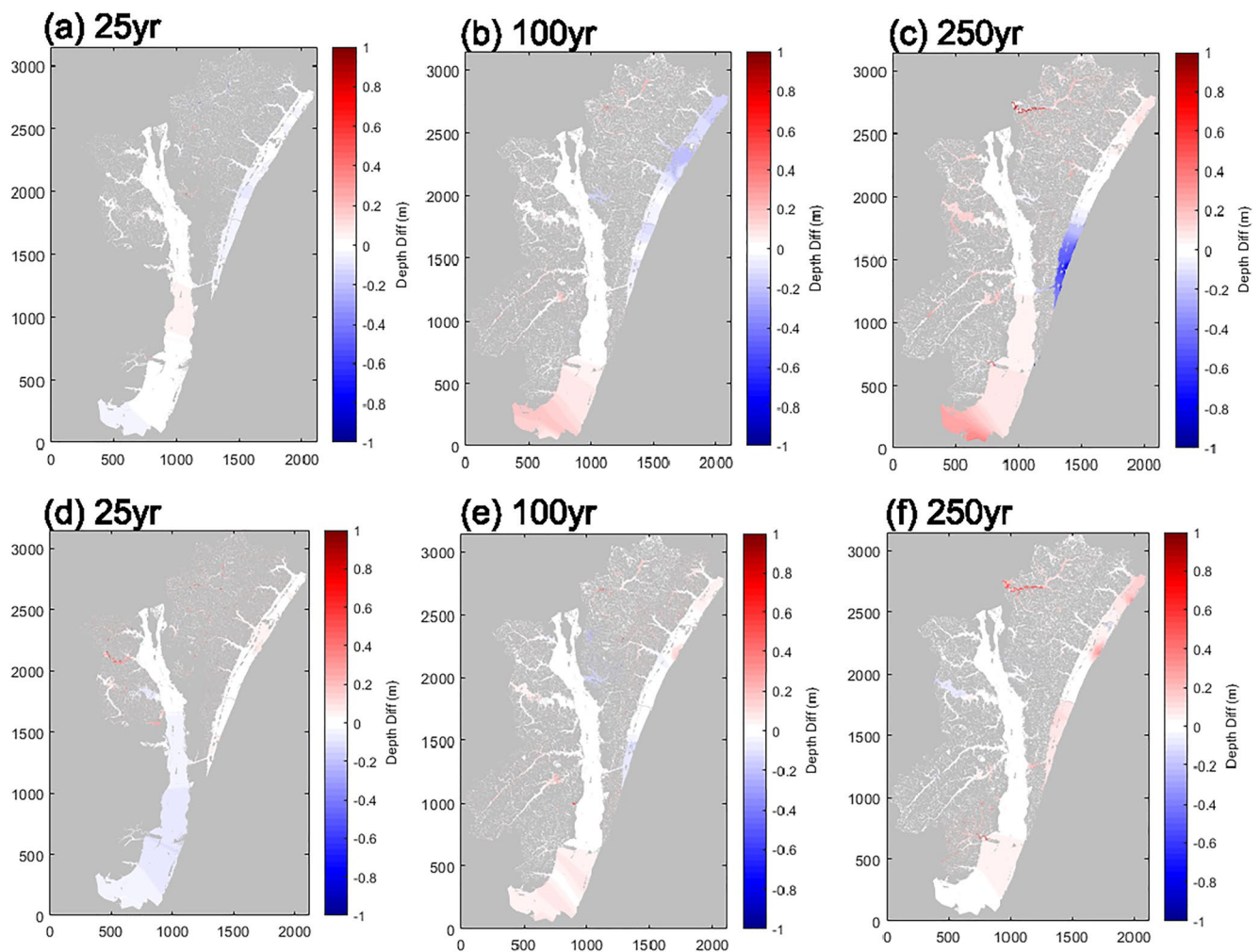
Figure 2. Flood height difference between Monte Carlo approach and joint probability optimal sampling Bayesian Quadrature (JPM-OS-BQ) approach for 25-year (a and d), 100-year (b and e), and 250-year (c and f) return levels. Top panels (a–c) depict results for Approach 1 and bottom panels (d–f) depict results for Approach 2. Negative values (blue) indicate JPM-OS-BQ overestimation and positive values (red) indicate underestimation.

hydrologic modeling system (HEC-HMS; HEC, 2016) and input as point boundary conditions at three locations within the flood model domain (Figure 1). Full details of the model framework are documented in Gori, Lin, and Smith (2020); Gori, Lin, and Xi (2020).

3. Results

3.1. Performance of JPM-OS-BQ Method for Compound Flood Assessment

To evaluate the use of the JPM-OS-BQ method for representing compound flood hazard, we compare flood maps generated using each of the two approaches against MC-based flood maps that were computed in Gori, Lin, and Xi et al. (2020). The MC flood maps use the same synthetic storm set as the JPM-OS-BQ approach and were generated by simulating each of the 941 synthetic events within the high-resolution flood model and then deriving return period flood maps based on the empirical distribution of water levels at each grid point in the study domain. As such, the MC maps represent a high-fidelity estimate of compound flood hazard in the study domain. Figure 2 shows maps of the flood height difference between the MC approach and JPM-OS-BQ approach for return periods ranging from 25 to 250 years. The top panels show comparison results for Approach 1 (utilizing storm parameters), while the bottom panels show results for Approach 2 (utilizing flood drivers). Areas of blue indicate JPM-OS-BQ overestimates peak water levels compared to the MC method, areas of white indicate no difference between approaches, and areas of red indicate that JPM-OS-BQ underestimates peak water levels.

Both JPM-OS-BQ approaches perform similarly well for the 25-year return level since the flood difference maps show most areas in white or light blue/red, which indicates small flood height difference between the JPM-OS-BQ and MC. For the 25-year level, Approach 1 matches 100% of the floodplain is within 0.25 m of the MC water levels and Approach 2 matches 99% of the floodplain is within 0.25 m. However, for the higher 100 and 250 years return periods, which represent more severe flooding conditions, Approach 2 performs better than Approach 1. For example, for the 100-year level Approach 2 matches the peak water level within 0.25 m for 99.7% of the floodplain. In contrast, although Approach 1 still matches peak water levels for 95% of the floodplain, it significantly underestimates (by more than 0.25 m) water levels at the mouth of the river while significantly overestimating water levels along the eastern coastline region (see areas of red/blue in Figure 2, respectively). The discrepancy in water levels for Approach 1 is likely due to the high weight placed on V_{max} in the JPM-OS-BQ optimization, whereas extreme storm tides are generated by a confluence of many additional factors, such as approach angle (not included here). The same spatial trend is more pronounced for the 250-year level, where water levels are underestimated by up to 0.4 m (17%) at the mouth of the river and overestimated by up to 0.5 m (22%) along the coastline. The return level comparison maps demonstrate that more accurate compound flood hazard results can be achieved by directly utilizing peak rainfall and storm tide within the JPM-OS-BQ framework, since both variables are highly correlated with peak water levels across the study domain. In contrast, while the TC storm parameters (i.e., V_{max}, R_{max}, etc.) are also correlated with peak water leslevels, the correlation is not as strong and consequently these parameters yield lower accuracy at high return periods. Despite the lower performance of Approach 1, the JPM-OS-BQ approach using storm parameters still captures the 250-year peak water levels within 0.25 m for over 95% of the floodplain area. Thus, if the modeled storm tides and rainfall rates are not available for the entire storm set (as in this study), the storm parameters may be used in the JPM-OS-BQ algorithm and still achieve reasonable hazard estimates.

After validating the JPM-OS-BQ approach using the NCEP storms for the historical period, we next apply the JPM-OS-BQ algorithm to select representative storms for the future period considering the projected 2100 SLR distribution and the CMIP6 synthetic storms. Due to the more accurate representation of historical compound flood hazard achieved by directly utilizing the flood drivers in the JPM-OS-BQ algorithm (Approach 2 in Figure 2), we adopt this approach for the analysis for the future period. Since MC-based flood maps do not exist for the future period (as this would require ~10,000 high-resolution flood simulations), we cannot compare the JPM-OS-BQ future flood maps against a set of reference flood maps. Here we evaluate how well the limited number of JPM-OS-BQ storms and their associated weights are able to represent the probability distributions of each parameter (i.e., rainfall, storm tide, time lag, SLR) in the physical parameter space. Due to the small number ($N = 120$) of selected storms relative to the entire storm set ($N \sim 10,000$) and due to the transformation of the joint probability function into a multivariate normal mixture distribution, the selected storms and their calculated weights cannot match the original joint distribution exactly. However, successful implementation of the JPM-OS-BQ approach would result in a good approximation of the distributions of each optimization parameter. Figure 3 shows a comparison of the cumulative probability distributions (CDFs) for the parameters of (a) peak rainfall rate, (b) peak storm tide, (c) time lag, and (d) SLR based on the full storm set (blue; ~10,000 storms) and based on the selected JPM-OS-BQ set (pink; 120 storms).

Across all parameters shown in Figure 3, the JPM-OS-BQ storms can well-represent the true CDFs, especially for the peak rainfall rate and peak storm tide. The JPM-OS-BQ storms can accurately match both the rainfall and storm tide distributions for their entire CDFs, including the heavy upper tail portion. This is due to the use of the normal mixture model in the optimization space, which gives non-negligible density to extreme storms, and allows extreme storms to be chosen and weighted accurately. Additionally, both the rainfall and storm tide had the smallest specified correlation distances ($c = 0.5$), corresponding to smaller spacing between storms in these dimensions and consequently more refined representation of their CDFs. The SLR distribution is also well matched by the JPM-OS-BQ storm set (Figure 3d), except for the lower tail, where there is some discrepancy between the two CDFs. The small discrepancy in the representation of the lower tail of the distribution is unlikely to have a significant impact on compound flood return levels, and it is due to the use of the two-component normal mixture model in the optimization space, which places more weight on the upper tail. The JPM-OS-BQ storms match the general shape of the time lag distribution (Figure 3c), although the CDF representation is coarse compared to the true CDF. This is because the time lag parameter had the highest correlation distance ($c = 2$), since it is a relatively small contributor to overall flooding compared to the other three parameters. The comparisons shown in Figure 3 demonstrate that the JPM-OS-BQ storms reproduce the true parameter distributions for the future period and thus are likely to yield a reasonable representation of projected compound flood hazard.
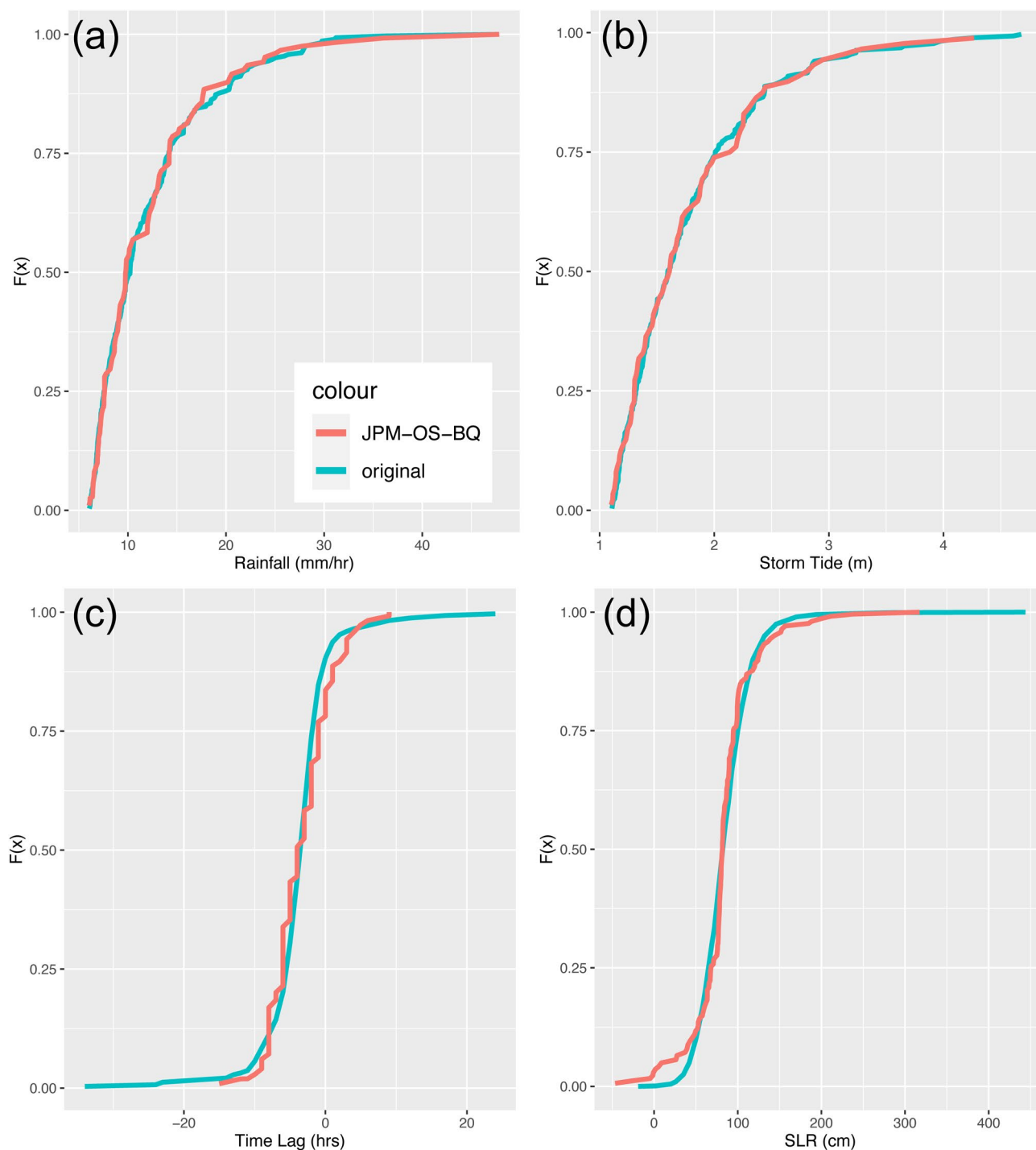
Figure 3. Cumulative probability distributions comparison between full storm set (blue) and joint probability optimal sampling Bayesian Quadrature limited storm set (pink) for (a) peak rainfall rate, (b) peak storm tide, (c) time lag, and (d) sea-level rise.

3.2. Impact of Climate Change on TC Hazards

Before investigating the impact of SLR and changing storm climatology on compound flooding, we first evaluate how peak rainfall rates and peak storm tides are projected to change in the Cape Fear region by the end of the 21st century under the highest emission scenario (SSP 5 8.5). Figure 4 shows return period curves for (a) the area-averaged peak storm tide and (b) the area-averaged peak rainfall rate in the historical period (black),
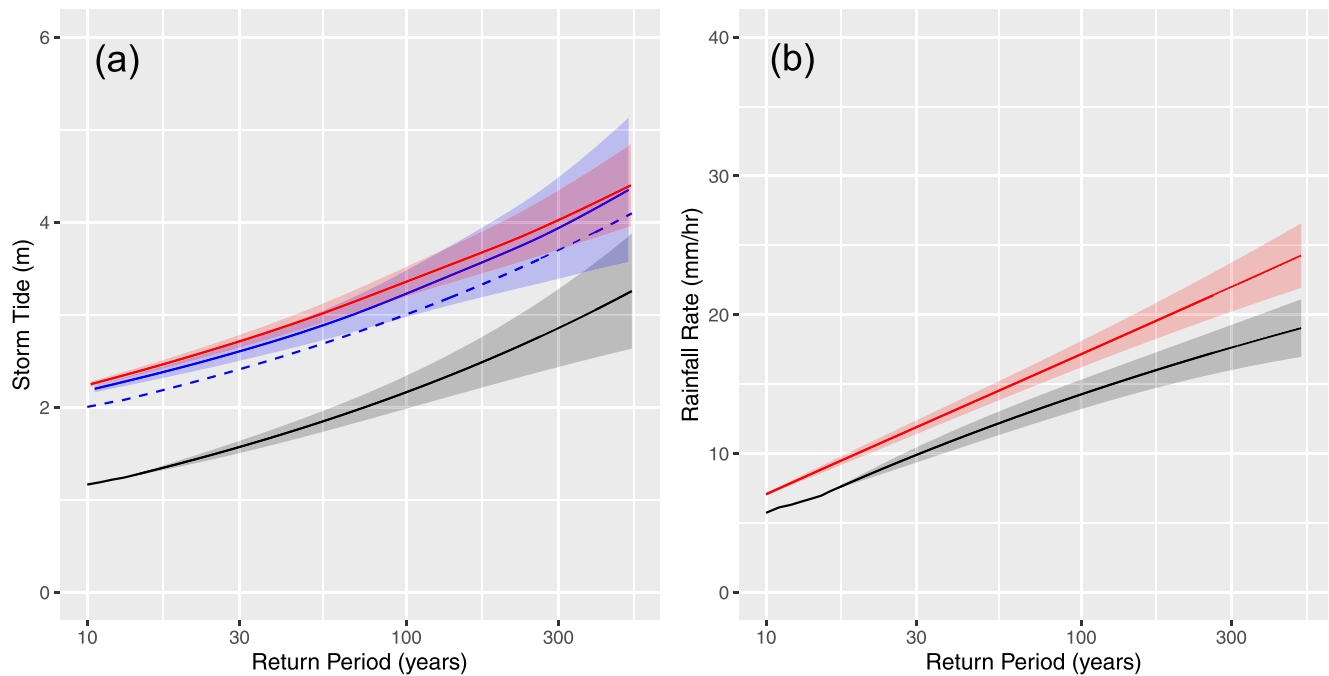
Figure 4. Return level curves under historical sea-level and climatology (black), future sea-level and historical climatology (blue) and future sea-level and future climatology (red) for (a) peak storm tide and (b) peak rainfall rate. Shaded areas depict 90% confidence bounds calculated through the Delta Method.

under future SLR (blue), and under future SLR plus future storm climatology change (red). The return period curves are constructed using the full synthetic data set rather than the limited JPM-OS storm set. Therefore, the storm tide curves that incorporate SLR are computed by convolving the TC-induced storm tide CDF with the SLR probability density function as in Lin et al. (2016) and Marsooli et al. (2019). The dashed blue line represents the historical storm tide return period curve plus the mean of the projected SLR (0.84 m). Importantly, the convolution-based storm tide curve is higher than the mean SLR curve because it takes into account the full heavy-tailed SLR distribution. At the 100-year level, the difference between the convolution-based curve (solid blue) and mean SLR curve (dashed blue) is 0.29 m.

The projected SLR is the main driver of increased future storm tide hazard across all return periods, but the future storm climatology change also causes a small additional increase in storm tide hazard (see red curve on Figure 4a). A previous study using the same TC model and a suite of CMIP5 GCMs found a larger contribution of TC climatology change to changes in storm tide hazard in the Cape Fear region (Marsooli et al., 2019) than we find here, although they found that SLR still contributes roughly 70% to future overall 100-year storm tide hazard. The difference between our results and those in Marsooli et al. (2019) mainly stems from our choice of neglecting TC frequency change in the calculation of the future storm tide hazard. Another reason for the discrepancy is due to our use of a different TC size generation methodology (Gori et al., 2022) that resulted in smaller synthetic TCs compared to those used in Marsooli et al. (2019).

In contrast to the relatively small climatology-induced increases to storm tide hazard, changes in TC climatology are projected to result in large increases in rainfall hazard by the end of the century (Figure 4b). The 50-year rainfall rate is projected to increase by 19%, the 250-year rainfall rate by 23%, and the 500-year rainfall rate by 27%. The larger projected increase in rainfall for higher return periods demonstrates that the upper tail of the rainfall distribution is projected to increase by more than the rest of the distribution, potentially yielding worse flooding impacts for high return periods.

3.3. Projected Change in Compound Flood Hazard

The large projected increases in rainfall rate and peak storm tides shown in Figure 4 cause severe and widespread increases in inundation extent and depth across the Cape Fear study area. Figure 5 shows the 100-year flood
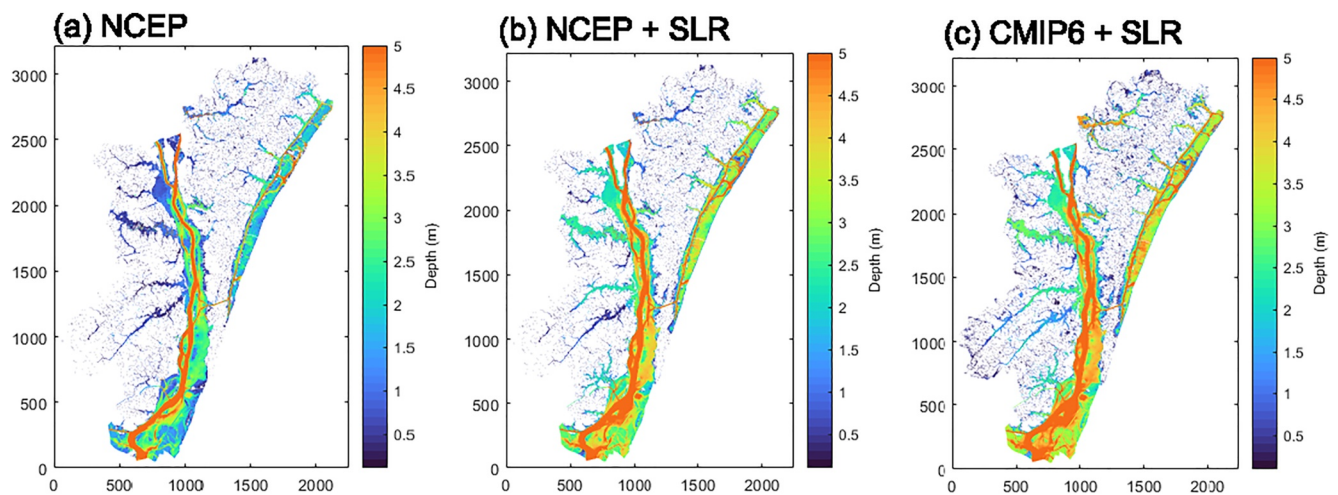
Figure 5. 100-year flood depths across the Cape Fear Estuary domain for the (a) National Centers for Environmental Prediction (NCEP) historical period (1980–2005), (b) NCEP storm climatology and 2100 sea level rise (SLR), and (c) for the future projected CMIP6 climatology (2070–2100) and 2100 SLR.

depths (calculated at each grid point) for (a) the historical period based on NCEP reanalysis data (referred to as NCEP), (b) the historical storm climatology and projected 2100 SLR (NCEP + SLR), and (c) the projected 2070–2100 storm climatology from the CMIP6 models and projected 2100 SLR (CMIP6 + SLR). The incorporation of future SLR in the calculation of 100-year flood depths (Figure 5b) results in large increases in peak water levels within the main stem of the river, along the low-lying coastal regions, and along the tributaries that drain to the Cape Fear River. Additionally, incorporating future storm climatology (Figure 5c) causes further increases in peak water levels along the coast, the river, and tributaries, as well as widespread increases in overland flooding extent (see increase in pluvial flooding shown in Figure 5c compared to Figure 5a). The severe increase in pluvial flooding is caused by large increases in rainfall rate (Figure 4b) and total rainfall accumulations that cannot be fully infiltrated or attenuated within the drainage basin. The additional increase in peak water levels within the river and tributaries caused by the projected storm climatology change is due to both increases in peak storm surges (Figure 4a) and the additional rainfall-runoff volume draining to the river system.

The impact of SLR and TC climatology change on changes in compound flooding varies across different return levels. Figure 6 shows the percent increase in (a) inundation extent (for inundation depths greater than 0.25 m) and (b) inundation volume for return periods between 10 and 250 years (calculated at each grid point), considering projected SLR alone (pink) and considering projected SLR plus projected TC climatology change (SLR + CMIP6) (blue). At the 10-year level, SLR causes a 25% increase in flood extent and SLR + CMIP6 causes a 43% increase. In contrast to the amplified increase in rain rate with increasing return period shown in Figure 4, the percent increase in flood extent decreases with increasing return period such that the 250-year level SLR causes only an 11% increase and SLR + CMIP6 causes a 26% increase. The reason for the diminishing increase in flood extent with increasing return period is due to features of the land topography: for lower return periods, low-lying areas that would previously have been dry are projected to become inundated due to either rainfall-runoff or upstream propagating SLR/storm tide, causing a large increase in inundation extent. However, for higher return periods, the majority of low-lying areas are already inundated in the historical period and the additional increases in rainfall-runoff and/or storm tides increase the depth of flooding in these areas but do not largely increase the flooding area. Figure 6b shows the percent increase in inundation volume, defined as the total volumetric increase in flood waters across the study domain. The percent increase in flood volume grows with increasing return level until 100 years for the SLR-only scenario and until 25 years for the SLR + CMIP6 scenario before leveling out at a constant increase, demonstrating that higher return periods drive large increases in flooding depth even though the increase in flooding extent is moderate. The SLR + CMIP6 scenario causes up to 64% increase in inundation volume at the 25-year level and the average increase in inundation volume across all return periods (59%) is higher than the largest projected increase in flood extent (43% at the 10-year level).

Although projected storm climatology change does cause a small increase in domain-averaged peak storm tides (Figure 4a), the majority of additional flood extent and depth increase under the SLR + CMIP6 scenario compared
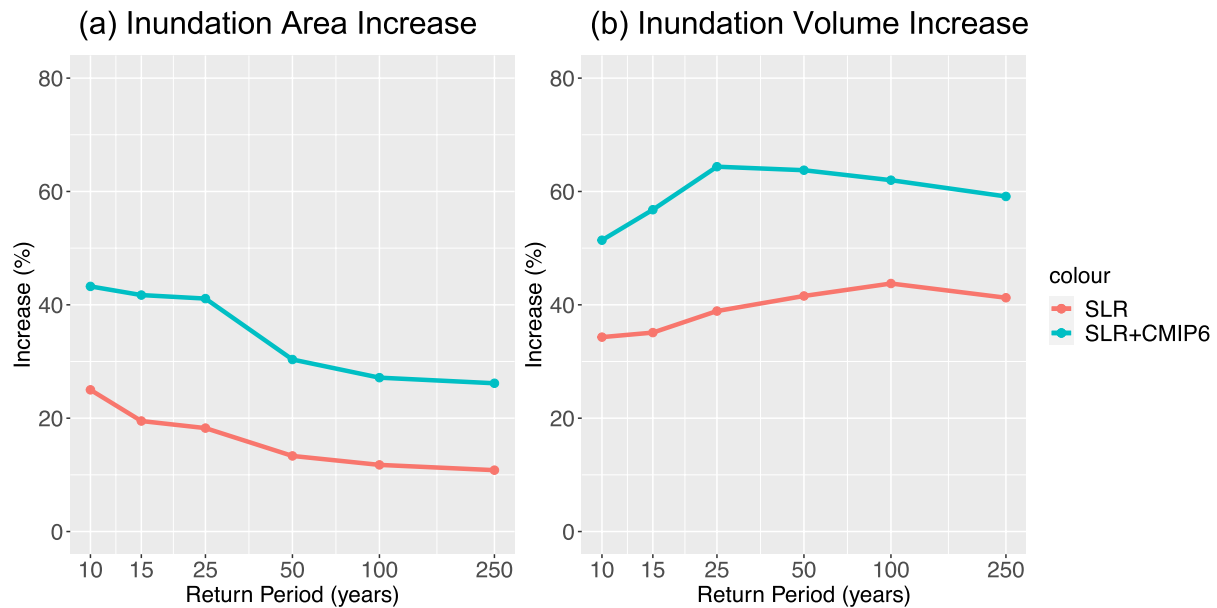
(a) Inundation Area Increase (b) Inundation Volume Increase

Figure 6. Compound flood increase due to sea-level rise (SLR)-only (pink) and SLR plus tropical cyclone climatology change (SLR + CMIP6; blue) measured by (a) percent increase in inundation area and (b) percent increase in inundation volume.

to the SLR-only scenario is due to increases in rainfall rates and rainfall totals, which increase pluvial flooding. Moreover, the combination of increased rainfall hazard and elevated river water levels due to SLR prevents efficient drainage of the basin, further increasing peak fluvial flood depths and extents. Previous studies have shown that projected SLR and/or increases in rainfall-runoff will increase the frequency of joint high sea-level and high discharge events (Ghanbari et al., 2021; Moftakhari et al., 2017) and here we show how increased frequency and severity of these types of events will translate to changes in coastal flooding extent and depth.

3.4. Impact of Probabilistic Versus Scenario-Based SLR

In our proposed methodology we incorporate SLR as an additional probabilistic parameter within the JPM-OS-BQ algorithm. Our approach differs from the majority of other coastal flood mapping studies that incorporate SLR by considering a limited set of scenarios, often using the mean/median projected increase (Bates et al., 2021; Bermúdez et al., 2021; Hamman et al., 2016). The use of a probabilistic SLR approach rather than Scenario-based approach can result in large differences in the projected coastal flood hazard. Figure 7 shows the difference in 100-year flood depths under historical TC climatology and 2100 SLR calculated using the probabilistic SLR approach (our method) compared to using the mean of the SLR projection. Areas of white indicate no difference in flood depths, while blues represent areas where probabilistic SLR flood depths are greater than mean SLR flood depths. In the overland areas and along the upper portions of small tributaries, where flooding is entirely driven by rainfall-runoff, there is no difference between the probabilistic and mean SLR approaches. Along the coastline and at the mouth of the river, the probabilistic SLR 100-year flood depths are 0.15–0.35 m higher than the mean SLR 100-year flood depths, which is consistent with the 0.29 m difference in area-averaged storm tide height between the two scenarios shown in Figure 4a. Within the main stem of the Cape Fear river and along its larger tributaries, the difference between the two approaches ranges from 0.5 to 0.6 m and reaches almost 1 m in water level difference for some upper tributary locations. The reason for the larger depth difference
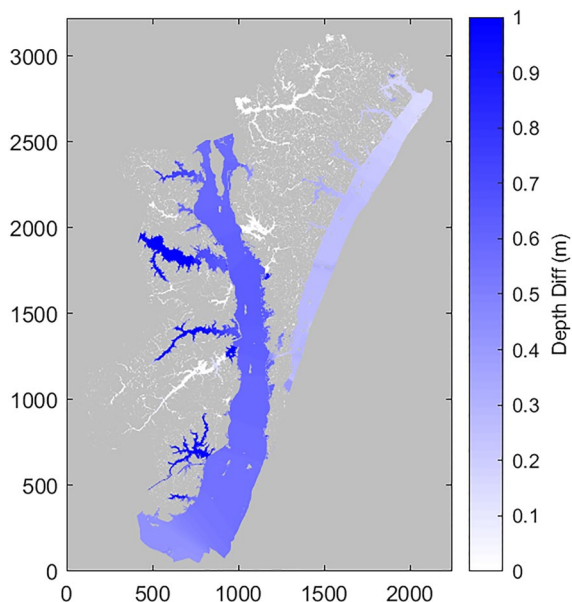

Figure 7. Difference in 100-year flood depths under historical tropical cyclone climatology and 2100 sea-level rise (SLR) using either probabilistic SLR or mean SLR. Positive values indicate areas where the probabilistic SLR flood depths are higher than the mean SLR flood depths.

within the main stem of the river and tidally influenced tributaries is likely due to the increased backwater effect caused by more extreme SLR realizations that were selected during the JPM-OS-BQ optimization. Within tidally influenced tributaries the increased backwater effect prevents drainage of the rainfall-runoff, exacerbating flooding and causing the largest depth differences between the probabilistic and mean SLR approaches. Our results show that differences in the specification of SLR within flood mapping approaches can lead to large differences in simulated flood hazard.

4. Discussion and Conclusions

In this study we propose an extension to the JPM-OS approach to evaluate compound flood hazard under evolving storm climatology and sea-level conditions. While many studies have implemented the JPM-OS method to evaluate storm surge hazard (Nadal-Caraballo et al., 2015; Niedoroda et al., 2008; Resio et al., 2009; Toro, Niedoroda, et al., 2010) and some studies have incorporated SLR in flood hazard analysis (Bilskie et al., 2019, 2022; Sheng et al., 2022), to our knowledge the JPM-OS method has not previously been applied to assess compound flood hazard from the combination of rainfall and storm tides. Traditionally, the JPM-OS approach has been applied to assign probabilities and weights to uniformly generated synthetic storms based on empirical marginal and joint distributions of storm parameters. One downside of this traditional approach is that the generated synthetic TC tracks may have parameter combinations that are not physically realistic. To overcome this limitation, here we utilize a set of synthetic TCs that were generated using a physics-based TC model and are consistent with the large-scale environment specified by NCEP reanalysis data. We then utilize the JPM-OS-BQ algorithm to select from the generated storm tracks, ensuring that all chosen tracks are physically realistic and consistent with a specified climate state. To apply the JPM-OS-BQ method for compound flood hazard assessment we utilize modeled rainfall fields and storm tides as optimization parameters rather than using TC storm characteristics, which yields a better approximation of compound flood return levels. In this work we specify the correlation distances in the autocovariance function based on previous literature and trial-and-error analysis. However, future work could implement a rigorous sensitivity analysis of the correlation distance parameters to understand how the JPM-OS-BQ model set up may potentially impact estimates of flood hazard. After developing compound flood maps for the historical period, we utilize modeled rainfall and storm tides based on a suite of CMIP6 GCMs to project the impact on compound flood hazard from changes in TC climatology and we incorporate SLR projections probabilistically. We show that SLR and increases in TC rainfall are the main drivers of future compound flood hazard and that the interaction of SLR and rainfall-runoff can significantly exacerbate riverine flood hazard in the future. Other studies have similarly found that SLR (Ghanbari et al., 2021; Moftakhari et al., 2017) and increased rainfall (Bevacqua et al., 2019; Gori et al., 2022) may drive large increases in the frequency of joint rainfall-surge extreme events, although our study is one of the first to investigate how changes in the frequency of rainfall-surge events will translate to changes in flooding depth and extent at different return periods. Finally, we demonstrate that incorporation of SLR as a probabilistic variable rather than a mean projection results in significant differences in 100-year compound flood depths, especially within the Cape Fear River and its tidally influenced tributaries. The difference in flood depths between the two approaches are spatially heterogenous across the study domain, suggesting that discrepancies between the two approaches cannot be easily reconciled by a simple plus/minus offset. We suggest future work investigate more thoroughly differences between scenario-based and probabilistic representations of SLR in flood mapping frameworks as they can lead to widely diverging flood hazard results in some locations.

Here we apply our modified JPM-OS-BQ approach to investigate flooding in the Cape Fear drainage basin, a single catchment in North Carolina. However, our approach could be applied to coastal catchments across the US Atlantic and Gulf coasts that are similarly vulnerable to compound flooding from TCs (such as the locations studied in Bilskie et al., 2021; Jane et al., 2020, 2022; Santos et al., 2021; Torres et al., 2015). Due to large uncertainty in projections of future TC frequency (Sobel et al., 2021), here we assume no change in storm frequency in the future period. Future work may conduct a sensitivity analysis to quantify how a variety of frequency change projections (i.e., frequency decrease vs. increase) would impact compound flood return levels. In the future, rainfall duration may increase as TC translation speed decreases (Emanuel, 2021; Yamaguchi et al., 2020; G. Zhang et al., 2020), potentially exacerbating peak flood levels. Therefore, future work may also investigate the use of alternate rainfall metrics, such as rain duration or rainfall total, in the JPM-OS-BQ algorithm. Alternately, the probability distribution of flood duration may be estimated using the JPM-OS-BQ approach. We focus on a single future warming scenario, the SSP5 8.5 high-emission pathway, but our results may be significantly differ-

ent under the moderate SSP2 4.5 pathway (Bacmeister et al., 2018; Bates et al., 2021; Bhatia et al., 2018; Liu et al., 2019). A complete understanding of future compound flood hazard requires consideration of a range of future pathways, and due to the computational efficiency of our approach, future work could incorporate flood hazard estimates for alternate SSPs and for differing time horizons. Moreover, the landscape and hydrology of coastal catchments may change in the future due to urbanization (Gori et al., 2019; Juan et al., 2020; Sebastian et al., 2019; W. Zhang et al., 2018), subsidence, and coastal land loss (Bilskie et al., 2014, 2016, 2022; Passeri et al., 2015), which may alter the dynamics of compound flooding. Our approach could be applied under a range of land use conditions to better anticipate the combined impact of climate and landscape change on coastal hazard. Finally, the compound flood hazard approach outlined here, which requires relatively few flood simulations, could be implemented to evaluate the effectiveness of proposed coastal infrastructure projects (Christian et al., 2015) probabilistically rather than deterministically.

Data Availability Statement

Floodplain projections generated in this study are published in Gori and Lin (2022) within the NSF DesignSafe-CI and can be freely assessed online (https://doi.org/10.17603/ds2-zr29-5253 or directly at https://www.designsafe-ci.org/data/browser/public/designsafe.storage.published/PRJ-3730). The codes used to conduct the JPM-OS-BQ optimization are also published in Gori and Lin (2022) within the NSF DesignSafe-CI and can be freely accessed online (https://doi.org/10.17603/ds2-zr29-5253 or at https://www.designsafe-ci.org/data/browser/public/designsafe.storage.published/PRJ-3730).

References

Arns, A., Wahl, T., Wolff, C., Vafeidis, A. T., Haigh, I. D., Woodworth, P., et al. (2020). Non-linear interaction modulates global extreme sea levels, coastal flood exposure, and impacts. *Nature Communications*, 11, 1–9. https://doi.org/10.1038/s41467-020-15752-5

Bacmeister, J. T., Reed, K. A., Hannay, C., Lawrence, P., Bates, S., Truesdale, J. E., et al. (2018). Projected changes in tropical cyclone activity under future warming scenarios using a high-resolution climate model. *Climate Change*, 146(3–4), 547–560. https://doi.org/10.1007/s10584-016-1750-x

Bass, B., & Bedient, P. (2018). Surrogate modeling of joint flood risk across coastal watersheds. *Journal of Hydrology*, 558, 159–173. https://doi.org/10.1016/j.jhydrol.2018.01.014

Bass, B., Juan, A., Gori, A., Fang, Z., & Bedient, P. B. (2016). 2015 memorial day storm flood impacts for changing watershed conditions in Houston, TX. *Natural Hazards Review*, 18(3), 1–11. https://doi.org/10.1061/(ASCE)NH.1527-6996.0000241

Bates, P. D., Quinn, N., Sampson, C., Smith, A., Wing, O., Sosa, J., et al. (2021). Combined modeling of US fluvial, pluvial, and coastal flood Hazard under current and future climates. *Water Resources Research*, 57(2), 1–29. https://doi.org/10.1029/2020WR028673

Bermúdez, M., Farfán, J. F., Willems, P., & Cea, L. (2021). Assessing the effects of climate change on compound flooding in coastal river areas. *Water Resources Research*, 57(10). https://doi.org/10.1029/2020WR029321

Bevacqua, E., Maraun, D., Vousdoukas, M. I., Voukouvalas, E., Vrac, M., Mentaschi, L., & Widmann, M. (2019). Higher probability of compound flooding from precipitation and storm surge in Europe under anthropogenic climate change. *Science Advances*, 5(9), 1–8. https://doi.org/10.1126/sciadv.aaw5531

Bhatia, K., Vecchi, G., Murakami, H., Underwood, S., & Kossin, J. (2018). Projected response of tropical cyclone intensity and intensification in a global climate model. *Journal of Climate*, 31(20), 8281–8303. https://doi.org/10.1175/JCLI-D-17-0898.1

Bilskie, M. V., Angel, D., Yoskowitz, D., & Hagen, S. C. (2022). Future flood risk exacerbated by the dynamic impacts of sea level rise along the Northern Gulf of Mexico. *Earth's Future*, 10(4). https://doi.org/10.1029/2021EF002414

Bilskie, M. V., Hagen, S. C., Alizad, K., Medeiros, S. C., Passeri, D. L., Needham, H. F., & Cox, A. (2016). Dynamic simulation and numerical analysis of hurricane storm surge under sea level rise with geomorphologic changes along the northern Gulf of Mexico. *Earth's Future*, 4(5), 177–193. https://doi.org/10.1002/2015EF000347

Bilskie, M. V., Hagen, S. C., & Irish, J. L. (2019). Development of return period Stillwater floodplains for the Northern Gulf of Mexico under the coastal dynamics of sea level rise. *Journal of Waterway, Port, Coastal, and Ocean Engineering*, 145(2), 1–14. https://doi.org/10.1061/(ASCE)WW.1943-5460.0000468

Bilskie, M. V., Hagen, S. C., Medeiros, S. C., & Passeri, D. L. (2014). Dynamics of sea level rise and coastal flooding on a changing landscape. *Geophysical Research Letters*, 41(3), 927–934. https://doi.org/10.1002/2013GL058759

Bilskie, M. V., Zhao, H., Resio, D., Atkinson, J., Cobell, Z., & Hagen, S. C. (2021). Enhancing flood Hazard assessments in coastal Louisiana through coupled Hydrologic and surge processes. *Frontiers in Water*, 3, 1–19. https://doi.org/10.3389/frwa.2021.609231

Bloemendaal, N., Haigh, I. D., de Moel, H., Muis, S., Haarsma, R. J., & Aerts, J. C. J. H. (2020). Generation of a global synthetic tropical cyclone hazard dataset using STORM. *Scientific Data*, 7(1), 40. https://doi.org/10.1038/s41597-020-0381-2

Booth, J. F., Rieder, H. E., & Kushnir, Y. (2016). Comparing hurricane and extratropical storm surge for the Mid-Atlantic and Northeast Coast of the United States for 1979-2013. *Environmental Research Letters*, 11(9), 094004. https://doi.org/10.1088/1748-9326/11/9/094004

Brunner, G. (2016). HEC-RAS, river analysis system Hydraulic reference manual.

Christian, J., Fang, Z., Torres, J. M., Dietz, R., & Bedient, P. B. (2015). Modeling the hydraulic effectiveness of a proposed storm surge barrier system for the Houston ship channel during Hurricane events. *Natural Hazards Review*, 16(1). https://doi.org/10.1061/(ASCE)NH.1527-6996.0000150

Condon, A. J., & Sheng, Y. P. (2012). Optimal storm generation for evaluation of the storm surge inundation threat. *Ocean Engineering*, 43, 13–22. https://doi.org/10.1016/j.oceaneng.2012.01.021

Couasnon, A., Eilander, D., Muis, S., Veldkamp, T. I. E., Haigh, I. D., Wahl, T., et al. (2019). Measuring compound flood potential from river discharge and storm surge extremes at the global scale and its implications for flood hazard. *Natural Hazards and Earth System Sciences Discussions*, 1–24. https://doi.org/10.5194/nhess-2019-205

Couasnon, A., Sebastian, A., & Morales-Nápoles, O. (2018). A Copula-based Bayesian network for modeling compound flood hazard from riverine and coastal interactions at the catchment scale: An application to the Houston ship channel Texas. *Water (Switzerland)*, *10*(9), 1190. https://doi.org/10.3390/w10091190

Emanuel, K. (2021). Response of global tropical cyclone activity to increasing CO2: Results from downscaling CMIP6 models. *Journal of Climate*, *34*(1), 57–70. https://doi.org/10.1175/JCLI-D-20-0367.1

Emanuel, K., DesAutels, C., Holloway, C., & Korty, R. (2004). Environmental control of tropical cyclone intensity. *Journal of the Atmospheric Sciences*, *61*(7), 843–858. https://doi.org/10.1175/1520-0469(2004)061<0843:ECOTCI>2.0.CO;2

Emanuel, K., Ravela, S., Vivant, E., & Risi, C. (2006). A statistical deterministic approach to Hurricane risk assessment. *Bulletin of the American Meteorological Society*, *87*(3), S1–S5. https://doi.org/10.1175/bams-87-3-emanuel

Emanuel, K., & Rotunno, R. (2011). Self-stratification of tropical cyclone outflow. Part I: Implications for storm structure. *Journal of the Atmospheric Sciences*, *68*(10), 2236–2249. https://doi.org/10.1175/JAS-D-10-05024.1

Famikhalili, R., & Talke, S. A. (2016). The effect of channel deepening on tides and storm surge: A case study of Wilmington, NC. *Geophysical Research Letters*, *43*(17), 9138–9147. https://doi.org/10.1002/2016GL069494

Feldmann, M., Emanuel, K., Zhu, L., & Lohmann, U. (2019). Estimation of Atlantic tropical cyclone rainfall frequency in the U.S. *Journal of Applied Meteorology and Climatology*, *58*(8), 1853–1866. https://doi.org/10.1175/JAMC-D-19-0011.1

FEMA. (2012). Joint probability—Optimal sampling method for tropical storm surge frequency analysis. *Operating Guidance*, 8–12.

Friedman, J., Hastie, T., & Tibshirani, R. (2010). Regularization paths for generalized linear models via coordinate descent. *JSS Journal of Statistical Software*, *33*(1). https://doi.org/10.18637/jss.v033.i01

Ghanbari, M., Arabi, M., Kao, S., Obeysekera, J., & Sweet, W. (2021). Climate change and changes in compound coastal-riverine flooding Hazard along the U.S. Coasts. *Earth's Future*, *9*(5). https://doi.org/10.1029/2021EF002055

Gori, A., Blessing, R., Juan, A., Brody, S., & Bedient, P. (2019). Characterizing urbanization impacts on floodplain through integrated land use, Hydrologic, and Hydraulic modeling. *Journal of Hydrology (Amsterdam)*, *568*, 82–95. https://doi.org/10.1016/j.jhydrol.2018.10.053

Gori, A., & Lin, N. (2022). *JPM-OS compound flooding*. DesignSafe-CI. https://doi.org/10.17603/ds2-zr29-5253v1

Gori, A., Lin, N., & Smith, J. (2020). Assessing compound flooding from landfalling tropical cyclones on the North Carolina coast. *Water Resources Research*, *56*(4). https://doi.org/10.1029/2019wr026788

Gori, A., Lin, N., & Xi, D. (2020). Tropical cyclone compound flood Hazard assessment: From investigating drivers to quantifying extreme water levels. *Earth's Future*, *8*(12). https://doi.org/10.1029/2020EF001660

Gori, A., Lin, N., Xi, D., & Emanuel, K. (2022). Tropical cyclone climatology change greatly exacerbates U. S extreme rainfall–surge hazard. *Nature Climate Change*, *12*(2), 171–178. https://doi.org/10.1038/s41558-021-01272-7

Green, W. H., & Ampt, G. (1911). Studies of soil physics, part I—The flow of air and water through soils. *Journal of Agricultural Sciences*, *4*, 1–24.

Hallegatte, S., Green, C., Nicholls, R. J., & Corfee-Morlot, J. (2013). Future flood losses in major coastal cities. *Nature Climate Change*, *3*(9), 802–806. https://doi.org/10.1038/nclimate1979

Hamman, A. J. J., Hamlet, A. F., Lee, S., Fuller, R., & Grossman, E. (2016). Combined effects of projected sea level rise, storm surge, and Peak River Flows on water levels in the Skagit floodplain. *Northwest Science*, *90*(1), 57–78. https://doi.org/10.3955/046.090.0106

HEC. (2016). Hydrologic Modeling System HEC-HMS Users Manual (Version 4.2).

Ho, F. P., & Myers, V. A. (1975). *Joint Probability Method of Tide Frequency Analysis Applied to Apalachicola Bay and St*. George Sound.

Holland, G. (1980). An analytical model of wind and pressure profiles in hurricanes. *Monthly Weather Review*, *108*(8), 1212–1218. https://doi.org/10.1175/1520-0493(1980)108<1212:aamotw>2.0.co;2

Holland, G. J. (1983). Tropical cyclone motion: Environmental interaction plus a beta effect. *Journal of the Atmospheric Sciences*, *40*(2), 328–342. https://doi.org/10.1175/1520-0469(1983)040<0328:tcmeip>2.0.co;2

Hsiao, S. C., Chiang, W. S., Jang, J. H., Wu, H. L., Lu, W. S., Chen, W. B., & Wu, Y. T. (2021). Flood risk influenced by the compound effect of storm surge and rainfall under climate change for low-lying coastal areas. *Science of the Total Environment*, *764*, 144439. https://doi.org/10.1016/j.scitotenv.2020.144439

Ikeuchi, H., Hirabayashi, Y., Yamazaki, D., Kiguchi, M., Koirala, S., Nagano, T., et al. (2015). Modeling complex flow dynamics of fluvial floods exacerbated by sea level rise in the Ganges-Brahmaputra-Meghna Delta. *Environmental Research Letters*, *10*(12), 124011. https://doi.org/10.1088/1748-9326/10/12/124011

Irish, J. L., & Resio, D. T. (2013). Method for estimating future hurricane flood probabilities and associated uncertainty. *Journal of Waterway, Port, Coastal, and Ocean Engineering*, *139*(2), 126–134. https://doi.org/10.1061/(ASCE)WW.1943-5460.0000157

Irish, J. L., Resio, D. T., & Cialone, M. A. (2009). A surge response function approach to coastal hazard assessment. Part 2: Quantification of spatial attributes of response functions. *Natural Hazards*, *51*(1), 183–205. https://doi.org/10.1007/s11069-009-9381-4

Jane, R., Cadavid, L., Obeysekera, J., & Wahl, T. (2020). Multivariate statistical modelling of the drivers of compound flood events in South Florida. *Natural Hazards and Earth System Sciences*, 1–30. https://doi.org/10.5194/nhess-2020-82

Jane, R., Wahl, T., Asce, A. M., Victor, Santos, M., Shubhra, et al. (2022). Assessing the potential for compound storm surge and extreme river discharge events at the catchment scale with statistical models: Sensitivity analysis and recommendations for best practice. https://doi.org/10.1061/(ASCE)HE.1943

Juan, A., Gori, A., & Sebastian, A. (2020). Comparing floodplain evolution in channelized and un-channelized urban watersheds in Houston, Texas. *Journal of Flood Risk Manag*, *13*(2). https://doi.org/10.1111/jfr3.12604

Kalnay, E., Collins, W., Deaven, D., Gandin, L., Iredell, M., Jenne, R., & Joseph, D. (1996). The NCEP_NCAR 40-year reanalysis project. *Bulletin of the American Meteorological Society*, *77*, 437–472. https://doi.org/10.1175/1520-0477(1996)077<0437:TNYRP>2.0.CO;2

Khanam, M., Sofia, G., Koukoula, M., Lazin, R., Nikolopoulos, E. I., Shen, X., & Anagnostou, E. N. (2021). Impact of compound flood event on coastal critical infrastructures considering current and future climate. *Natural Hazards and Earth System Sciences*, *21*(2), 587–605. https://doi.org/10.5194/nhess-21-587-2021

Kim, H., Villarini, G., Jane, R., Wahl, T., Misra, S., & Michalek, A. (2022). On the generation of high-resolution probabilistic design events capturing the joint occurrence of rainfall and storm surge in coastal basins. *International Journal of Climatology*. https://doi.org/10.1002/joc.7825

Kirezci, E., Young, I. R., Ranasinghe, R., Muis, S., Nicholls, R. J., Lincke, D., & Hinkel, J. (2020). Projections of global-scale extreme sea levels and resulting episodic coastal flooding over the 21st Century. *Scientific Reports*, *10*, 1–12. https://doi.org/10.1038/s41598-020-67736-6

Knutson, T., Camargo, S. J., Chan, J. C. L., Emanuel, K., Ho, C. H., Kossin, J., et al. (2020). Tropical cyclones and climate change assessment part II: Projected response to anthropogenic warming. *Bulletin of the American Meteorological Society*, *100*(10), 1987–2007. https://doi.org/10.1175/BAMS-D-18-0189.1

Kopp, R. E., DeConto, R. M., Bader, D. A., Hay, C. C., Horton, R. M., Kulp, S., et al. (2017). Evolving understanding of Antarctic ice-sheet physics and ambiguity in probabilistic sea-level projections. *Earth's Future*, *5*(12), 1217–1233. https://doi.org/10.1002/2017EF000663

Kopp, R. E., Horton, R. M., Little, C. M., Mitrovica, J. X., Oppenheimer, M., Rasmussen, D. J., et al. (2014). Probabilistic 21st and 22nd century sea-level projections at a global network of tide-gauge sites. *Earth's Future*, *2*(8), 383–406. https://doi.org/10.1002/2014ef000239

Kossin, J. P. (2018). A global slowdown of tropical-cyclone translation speed. *Nature*, *558*(7708), 104–107. https://doi.org/10.1038/s41586-018-0158-3

Lai, Y., Li, J., Gu, X., Liu, C., & Chen, Y. D. (2021). Global compound floods from precipitation and storm surge: Hazards and the roles of cyclones. *Journal of Climate*, 1–55. https://doi.org/10.1175/jcli-d-21-0050.1

Lian, J. J., Xu, K., & Ma, C. (2013). Joint impact of rainfall and tidal level on flood risk in a coastal city with a complex river network: A case study of Fuzhou city, China. *Hydrology and Earth System Sciences*, *17*(2), 679–689. https://doi.org/10.5194/hess-17-679-2013

Lin, N., Emanuel, K., Oppenheimer, M., & Vanmarcke, E. (2012). Physically based assessment of Hurricane surge threat under climate change. *Nature Climate Change*, *2*(6), 462–467. https://doi.org/10.1038/nclimate1389

Lin, N., Emanuel, K. A., Smith, J. A., & Vanmarcke, E. (2010). Risk assessment of hurricane storm surge for New York City. *Journal of Geophysical Research*, *115*(D18), 1–11. https://doi.org/10.1029/2009JD013630

Lin, N., Kopp, R. E., Horton, B. P., & Donnelly, J. P. (2016). Hurricane Sandy's flood frequency increasing from year 1800 to 2100. *Proceedings of the National Academy of Sciences*, *113*(43), 12071–12075. https://doi.org/10.1073/pnas.1604386113

Liu, M., Vecchi, G. A., Smith, J. A., & Knutson, T. R. (2019). Causes of large projected increases in hurricane precipitation rates with global warming. *NPJ Climate and Atmospheric Science*, *2*, 1–5. https://doi.org/10.1038/s41612-019-0095-3

Lombardo, F. T., Main, J. A., & Simiu, E. (2009). Automated extraction and classification of thunderstorm and non-thunderstorm wind data for extreme-value analysis. *Journal of Wind Engineering and Industrial Aerodynamics*, *97*(3–4), 120–131. https://doi.org/10.1016/j.jweia.2009.03.001

Lu, P., Lin, N., Emanuel, K., Chavas, D., & Smith, J. (2018). Assessing Hurricane rainfall mechanisms using a physics-based model: Hurricanes Isabel (2003) and Irene (2011). *Journal of the Atmospheric Sciences*, *75*(7), 2337–2358. https://doi.org/10.1175/jas-d-17-0264.1

Luettich, R. A., Westerink, J. J., & Scheffner, N. W. (1992). *ADCIRC: An advanced three-dimensional circulation model for shelves, coasts, and estuaries: Theory and methodology of ADCIRC-2DDI and ADCIRC-3DL*. Report 1.

Marsooli, R., & Lin, N. (2018). Numerical modeling of Historical storm tides and waves and their interactions along the U.S. East and Gulf coasts. *Journal of Geophysical Research: Oceans*, *123*(5), 3844–3874. https://doi.org/10.1029/2017JC013434

Marsooli, R., Lin, N., Emanuel, K., & Feng, K. (2019). Climate change exacerbates hurricane flood hazards along US Atlantic and Gulf Coasts in spatially varying patterns. *Nature Communications*, *10*, 1–9. https://doi.org/10.1038/s41467-019-11755-z

Ming, X., Liang, Q., Dawson, R., Xia, X., & Hou, J. (2022). A quantitative multi-hazard risk assessment framework for compound flooding considering hazard inter-dependencies and interactions. *Journal of Hydrology (Amsterdam)*, *607*, 127477. https://doi.org/10.1016/j.jhydrol.2022.127477

Minka, T. (2000). Deriving quadrature rules from Gaussian processes.

Moftakhari, H. R., Salvadori, G., AghaKouchak, A., Sanders, B. F., & Matthew, R. A. (2017). Compounding effects of sea level rise and fluvial flooding. *Proceedings of the National Academy of Sciences*, *114*(37), 9785–9790. https://doi.org/10.1073/pnas.1620325114

Moftakhari, H. R., Schubert, J. E., Aghakouchak, A., Matthew, R. A., & Sanders, B. F. (2019). Linking statistical and hydrodynamic modeling for compound flood hazard assessment in tidal channels and estuaries. *Advances in Water Resources*, *128*, 28–38. https://doi.org/10.1016/j.advwatres.2019.04.009

Muis, S., Verlaan, M., Winsemius, H. C., Aerts, J. C. J. H., & Ward, P. J. (2016). A global reanalysis of storm surges and extreme sea levels. *Nature Communications*, *7*(1), 11969. https://doi.org/10.1038/ncomms11969

Myers, V. A. (1975). Storm tide frequencies on the South Carolina Coast. In *NOAA technical rep. NWS-16*. U.S. Department of Commerce.

Nadal-Caraballo, N. C., Melby, J. A., Gonzalez, V. M., & Cox, A. T. (2015). Coastal storm hazards from Virginia to Maine, North Atlantic coast comprehensive study (NACCS).

Niedoroda, A. W., Resio, D. T., Toro, G., Divoky, D., & Reed, C. (2008). Efficient strategies for the joint probability evaluation of storm surge hazards. In *Solutions to coastal disasters congress 2008* (pp. 242–255).

Orton, P. M., Conticello, F. R., Cioffi, F., Hall, T. M., Georgas, N., Lall, U., et al. (2018). Flood hazard assessment from storm tides, rain and sea level rise for a tidal river estuary. *Natural Hazards*, *102*(2), 729–757. https://doi.org/10.1007/s11069-018-3251-x

Pasquier, U., He, Y., Hooton, S., Goulden, M., & Hiscock, K. M. (2018). An integrated 1D–2D hydraulic modelling approach to assess the sensitivity of a coastal region to compound flooding hazard under climate change. *Natural Hazards*, *98*(3), 0123456789–0123456937. https://doi.org/10.1007/s11069-018-3462-1

Passeri, D. L., Hagen, S. C., Medeiros, S. C., Bilskie, M., Alizad, K., & Wang, D. (2015). The dynamic effects of sea level rise on low-gradient coastal landscapes: A review. *Earth's Future*, *3*(6), 159–181. https://doi.org/10.1002/2015EF000298.Received

Powell, M. J. D. (2004). The NEWUOA software for unconstrained optimization without derivatives 1. In *40th workshop on large scale nonlinear optimization*. Erice.

Resio, D. T., Irish, J., & Cialone, M. (2009). A surge response function approach to coastal hazard assessment—Part 1: Basic concepts. *Natural Hazards*, *51*(1), 163–182. https://doi.org/10.1007/s11069-009-9379-y

Rosenblatt, M. (1952). Remarks on a multivariate transformation. *The Annals of Mathematical Statistics*, *23*(3), 470–472. https://doi.org/10.1214/aoms/1177729394

Santos, V. M., Wahl, T., Jane, R., Misra, S. K., & White, K. D. (2021). Assessing compound flooding potential with multivariate statistical models in a complex estuarine system under data constraints. *Journal of Flood Risk Manag*, *14*(4). https://doi.org/10.1111/jfr3.12749

Schepsmeier, U., Stoeber, J., Brechmann, E. C., Graeler, B., Nagler, T., & Erhardt, T. (2016). Vinecopula: Statistical inference of vine copulas.

Schwalm, C. R., Glendon, S., & Duffy, P. B. (2020). RCP8.5 tracks cumulative CO_2 emissions. *Proceedings of the National Academy of Sciences of the United States of America*, *117*(33), 19656–19657. https://doi.org/10.1073/PNAS.2007117117

Sebastian, A., Gori, A., Blessing, R. B., van der Wiel, K., & Bass, B. (2019). Disentangling the impacts of human and environmental change on catchment response during Hurricane Harvey. *Environmental Research Letters*, *14*(12), 124023. https://doi.org/10.1088/1748-9326/ab5234

Serafin, K. A., Ruggiero, P., Parker, K. A., & Hill, D. F. (2019). What's streamflow got to do with it? A probabilistic simulation of the competing oceanographic and fluvial processes driving extreme along-river water levels. *Natural Hazards and Earth System Sciences Discussions*, 1–30. https://doi.org/10.5194/nhess-2018-347

Shen, Y., Morsy, M. M., Huxley, C., Tahvildari, N., & Goodall, J. L. (2019). Flood risk assessment and increased resilience for coastal urban watersheds under the combined impact of storm tide and heavy rainfall. *Journal of Hydrology (Amsterdam)*, *579*, 124159. https://doi.org/10.1016/j.jhydrol.2019.124159

Sheng, Y. P., Yang, K., & Paramygin, V. A. (2022). Predicting compound coastal inundation in 2100 by considering the joint probabilities of landfalling tropical cyclones and sea-level rise. *Environmental Research Letters*, *17*(4), 044055. https://doi.org/10.1088/1748-9326/ac50d1

Smith, J. A., Villarini, G., & Baeck, M. L. (2011). Mixture distributions and the Hydroclimatology of extreme rainfall and flooding in the Eastern United States. *Journal of Hydrometeorology*, *12*(2), 294–309. https://doi.org/10.1175/2010jhm1242.1

Sobel, A. H., Wing, A. A., Camargo, S. J., Patricola, C. M., Vecchi, G. A., Lee, C. Y., & Tippett, M. K. (2021). Tropical cyclone frequency. *Earth's Future*, *9*(12). https://doi.org/10.1029/2021EF002275

Stewart, S. R., & Berg, R. (2018). *Tropical cyclone report*. Hurricane Florence.

Toro, G. R., Niedoroda, A. W., Reed, C. W., & Divoky, D. (2010a). Quadrature-based approach for the efficient evaluation of surge hazard. *Ocean Engineering*, *37*(1), 114–124. https://doi.org/10.1016/j.oceaneng.2009.09.005

Toro, G. R., Resio, D. T., Divoky, D., Niedoroda, A. W., & Reed, C. (2010b). Efficient joint-probability methods for hurricane surge frequency analysis. *Ocean Engineering*, *37*(1), 125–134. https://doi.org/10.1016/j.oceaneng.2009.09.004

Torres, J. M., Bass, B., Irza, N., Fang, Z., Proft, J., Dawson, C., et al. (2015). Characterizing the hydraulic interactions of hurricane storm surge and rainfall-runoff for the Houston-Galveston region. *Coastal Engineering*, *106*, 7–19. https://doi.org/10.1016/j.coastaleng.2015.09.004

van den Hurk, B., van Meijgaard, E., de Valk, P., van Heeringen, K. J., & Gooijer, J. (2015). Analysis of a compounding surge and precipitation event in The Netherlands. *Environmental Research Letters*, *10*(3), 035001. https://doi.org/10.1088/1748-9326/10/3/035001

Villarini, G., Goska, R., Smith, J. A., & Vecchi, G. A. (2014). North Atlantic tropical cyclones and U.S. flooding. *Bulletin of the American Meteorological Society*, *95*(9), 1381–1388. https://doi.org/10.1175/BAMS-D-13-00060.1

Wahl, T., Jain, S., Bender, J., Meyers, S. D., & Luther, M. E. (2015). Increasing risk of compound flooding from storm surge and rainfall for major US cities. *Nature Climate Change*, *5*(12), 1–6. https://doi.org/10.1038/NCLIMATE2736

Wang, S. Y. S., Zhao, L., & Gillies, R. R. (2016). Synoptic and quantitative attributions of the extreme precipitation leading to the August 2016 Louisiana flood. *Geophysical Research Letters*, *43*(22), 11805–11814. https://doi.org/10.1002/2016GL071460

Ward, P. J., Couasnon, A., Eilander, D., Haigh, I. D., Hendry, A., Muis, S., et al. (2018). Dependence between high sea-level and high river discharge increases flood hazard in global deltas and estuaries. *Environmental Research Letters*, *13*(8), 084012. https://doi.org/10.1088/1748-9326/aad400

Westerink, J. J., Luettich, R. A., Blain, C. A., & Scheffner, N. W. (1992). *ADCIRC: An advanced three-dimensional circulation model for shelves, coasts, and estuaries: User's Manual for ADCIRC-2DDI*. Report 2.

Woodruff, J. D., Irish, J. L., & Camargo, S. J. (2013). Coastal flooding by tropical cyclones and sea-level rise. *Nature*, *504*(7478), 44–52. https://doi.org/10.1038/nature12855

Xi, D., Lin, N., & Smith, J. (2020). Evaluation of a physics-based tropical cyclone rainfall model for risk assessment. *Journal of Hydrometeorology*, *21*(9), 2197–2218. https://doi.org/10.1175/JHM-D-20-0035.1

Yamaguchi, M., Chan, J. C. L., Moon, I. J., Yoshida, K., & Mizuta, R. (2020). Global warming changes tropical cyclone translation speed. *Nature Communications*, *11*, 1–7. https://doi.org/10.1038/s41467-019-13902-y

Ye, F., Huang, W., Zhang, Y. J., Moghimi, S., Myers, E., Pe'eri, S., & Yu, H. C. (2021). A cross-scale study for compound flooding processes during Hurricane Florence. *Natural Hazards and Earth System Sciences*, *21*(6), 1703–1719. https://doi.org/10.5194/nhess-21-1703-2021

Yin, K., Xu, S., & Huang, W. (2018). Estimating extreme sea levels in Yangtze estuary by quadrature joint probability optimal sampling method. *Coastal Engineering*, *140*, 331–341. https://doi.org/10.1016/j.coastaleng.2018.08.007

Zellou, B., & Rahali, H. (2019). Assessment of the joint impact of extreme rainfall and storm surge on the risk of flooding in a coastal area. *Journal of Hydrology (Amsterdam)*, *569*, 647–665. https://doi.org/10.1016/j.jhydrol.2018.12.028

Zhang, G., Murakami, H., Knutson, T. R., Mizuta, R., & Yoshida, K. (2020). Tropical cyclone motion in a changing climate. *Science Advances*, *6*(17), 1–8. https://doi.org/10.1126/sciadv.aaz7610

Zhang, W., Villarini, G., Vecchi, G. A., & Smith, J. A. (2018). Urbanization exacerbated the rainfall and flooding caused by Hurricane Harvey in Houston. *Nature*, *563*(7731), 384–388. https://doi.org/10.1038/s41586-018-0676-z

Zhu, L., Emanuel, K., & Quiring, S. M. (2021). Elevated risk of tropical cyclone precipitation and pluvial flood in Houston under global warming. *Environmental Research Letters*, *16*(9), 094030. https://doi.org/10.1088/1748-9326/ac1e3d

Zhu, L., & Quiring, S. M. (2013). Variations in tropical cyclone precipitation in Texas (1950–2009). *Journal of Geophysical Research: Atmospheres*, *118*(8), 3085–3096. https://doi.org/10.1029/2012JD018554

Zhu, L., Quiring, S. M., & Emanuel, K. A. (2013). Estimating tropical cyclone precipitation risk in Texas. *Geophysical Research Letters*, *40*(23), 6225–6230. https://doi.org/10.1002/2013GL058284

Zscheischler, J., Martius, O., Westra, S., Bevacqua, E., Raymond, C., Horton, R. M., et al. (2020). A typology of compound weather and climate events. *Nature Reviews Earth & Environment*, *1*(7), 333–347. https://doi.org/10.1038/s43017-020-0060-z